Saarakkala, Seppo E.; Hinkkanen, Marko

# State-space speed control of two-mass mechanical systems: Analytical tuning and experimental evaluation

*Published in:*
IEEE Transactions on Industry Applications

*DOI:*
10.1109/TIA.2014.2306977

Published: 16/09/2014

*Document Version*
Peer-reviewed accepted author manuscript, also known as Final accepted manuscript or Post-print

*Please cite the original version:*
Saarakkala, S. E., & Hinkkanen, M. (2014). State-space speed control of two-mass mechanical systems: Analytical tuning and experimental evaluation. *IEEE Transactions on Industry Applications*, *50*(5), 3428-3437. https://doi.org/10.1109/TIA.2014.2306977

# State-Space Speed Control of Two-Mass Mechanical Systems: Analytical Tuning and Experimental Evaluation

Seppo E. Saarakkala and Marko Hinkkanen, *Senior Member, IEEE*

***Abstract*—This paper proposes a model-based two-degrees-of-freedom (2DOF) state-space speed controller design for a two-mass mechanical system. Analytical tuning rules for a feedback gain, reduced-order state observer, full-order state observer, and prefilter are derived. The proposed design rules enable automatic tuning of the controller if the mechanical parameters are known. The prefilter is designed for step, ramp, and parabolic command tracking. The effects of the time delay, measurement noise, and parameter variations on controller tuning and control performance are studied by means of Nyquist diagrams, noise transfer functions, and time-domain simulations. It is shown that the full-order observer based controller is a preferable choice, especially if the feedback loop is delayed and noisy. The proposed controller design is experimentally evaluated using two 4-kW servo motors coupled with toothed belt; good reference tracking for step and dynamic commands as well as robust and fast load-torque rejection is demonstrated.**

***Index Terms*—Delay, observer, resonance, stability, speed control, state-space control, two-mass system.**

## I. INTRODUCTION

High-performance ac electric drives are replacing pneumatic and hydraulic actuators or dc motor drives in modern machineries—such as injection molding machines [1], machine tools [2], and industrial robots [3]—due to their energy efficiency, compact size, and flexible control algorithms. These machineries often consist of several moving or rotating masses, which are coupled together with flexible mechanical transmissions (e.g., belts, gearboxes, long shafts), leading to mechanical resonances.

Resonant mechanical systems are commonly modeled as two-mass systems and controlled by means of 2DOF control, where regulation and command tracking are separately designed [2], [4]. The feedback controller is used to stabilize the feedback loop and to reject the loading torque (such as friction) acting on the system. The types of feedback controllers can be roughly categorized into five groups:

1) proportional integral (PI) or PI derivative (PID) controller [5]–[10];
2) PI controller augmented with additional feedbacks [5], [8], [11], [12];
3) PI controller and output filtering [5], [13]–[15];
4) state-feedback controller [4], [6], [16], [17];
5) nonlinear control methods such as sliding-mode [18], neuron-based [11], model-predictive [6], and repetitive [19] controllers.

The main advantage of the PI-type controller is straightforward tuning. However, if using solely the PI controller, only two of the four closed-loop poles can be freely placed. This is the reason why the PI controller may be augmented with additional feedbacks (e.g., load speed, motor or load acceleration, or estimated load disturbance) or the controller output may be filtered. On the other hand, if the state-feedback controller is used, all the closed-loop poles can be freely selected. A drawback of the state-feedback controller is that all the states have to be known.

As mentioned, it is appropriate to use the feedback controller only for the feedback-loop stabilization. If the feedback controller is designed for command tracking, the feedback gain increases and the stability may be lost. Instead, a feedforward controller (or a prefilter) inserted into the command path can be used to improve the command-tracking capability [2], [4], [9], [20]–[22]. The input command shaping may be used to generate the motion profiles [22]–[27].

In this paper, a complete model-based analytical design method for 2DOF state-space speed control of a two-mass system is proposed. The main contributions of this paper are:

1) Analytical design rules of the state-space controller (including the feedback gain, state observer, and prefilter) are presented.
2) A comparison of robustness between a full-order observer and a reduced-order observer is carried out. A special attention is paid to the sensitivity to the feedback-loop time delay and to the measurement-noise amplification.
3) Guidelines for the closed-loop pole selection, when the feedback loop is delayed, are proposed.
4) Performance and robustness of the proposed state-space controller is compared to those of the PI controller.

Similar design rules for the feedback gain have been proposed in [4], [6], [16], but the analysis of the feedback-loop time delay is omitted. Furthermore, according to the authors' knowledge, analytical design rules for the state observer and the prefilter have not been proposed before. Together with mechanical parameter estimation routine [28], the proposed control method can be easily used for automatic controller tuning.

S. E. Saarakkala and M. Hinkkanen are with the Dept. of Electrical Engineering, Aalto University, FI-00076 Aalto, Finland (e-mail: (seppo.saarakkala@aalto.fi, marko.hinkkanen@aalto.fi)

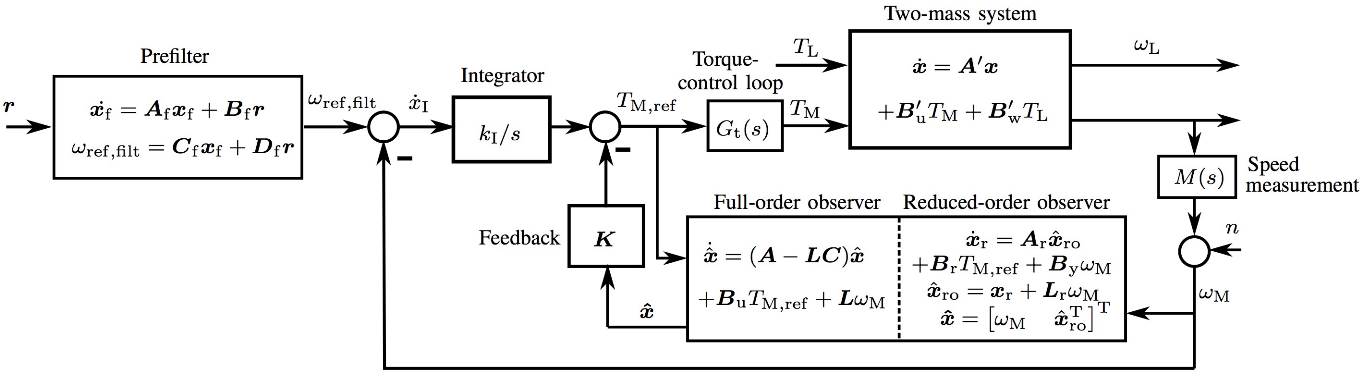

Fig. 1. 2DOF state-space speed control structure. The state-feedback can be constructed using a full-order or a reduced-order observer.

## II. SYSTEM MODEL

The mechanical dynamics of the resonating two-mass system are given as a state-space representation

$$\dot{\boldsymbol{x}} = \underbrace{\begin{bmatrix} -\frac{c'_\mathrm{S}}{J'_\mathrm{M}} & -\frac{K'_\mathrm{S}}{J'_\mathrm{M}} & \frac{c'_\mathrm{S}}{J'_\mathrm{M}} \\ 1 & 0 & -1 \\ \frac{c'_\mathrm{S}}{J'_\mathrm{L}} & \frac{K'_\mathrm{S}}{J'_\mathrm{L}} & -\frac{c'_\mathrm{S}}{J'_\mathrm{L}} \end{bmatrix}}_{\boldsymbol{A}'} \boldsymbol{x} + \underbrace{\begin{bmatrix} \frac{1}{J'_\mathrm{M}} \\ 0 \\ 0 \end{bmatrix}}_{\boldsymbol{B}'_\mathrm{u}} T_\mathrm{M} + \underbrace{\begin{bmatrix} 0 \\ 0 \\ -\frac{1}{J'_\mathrm{L}} \end{bmatrix}}_{\boldsymbol{B}'_\mathrm{w}} T_\mathrm{L} \tag{1}$$

where $\boldsymbol{x} = \begin{bmatrix}\omega_\mathrm{M} & \theta_\mathrm{M} - \theta_\mathrm{L} & \omega_\mathrm{L}\end{bmatrix}^\mathrm{T}$. The angular speeds of the motor and the load are $\omega_\mathrm{M}$ and $\omega_\mathrm{L}$, respectively. The motor electromagnetic torque is $T_\mathrm{M}$ and the loading torque is $T_\mathrm{L}$. The angular positions of the motor and the load are $\theta_\mathrm{M}$ and $\theta_\mathrm{L}$, respectively. The moments of inertias of the motor and the load are denoted as $J'_\mathrm{M}$ and $J'_\mathrm{L}$, respectively. The torsional stiffness and the damping of the shaft are $K'_\mathrm{S}$ and $c'_\mathrm{S}$, respectively. The symbol $'$ is used to refer to the actual values of the system parameters. In the following, the estimates of the system parameters will be marked without $'$. If $c_\mathrm{S} = 0$ is assumed, the antiresonance and resonance frequencies are estimated as

$$\omega_\mathrm{ares} = \sqrt{\frac{K_\mathrm{S}}{J_\mathrm{L}}}, \qquad \omega_\mathrm{res} = \sqrt{K_\mathrm{S}\frac{J_\mathrm{M} + J_\mathrm{L}}{J_\mathrm{M}J_\mathrm{L}}} \tag{2}$$

respectively.

## III. SPEED CONTROLLER DESIGN

The speed controller, depicted in Fig. 1, is designed in this section under the following assumptions: the estimate of the torsional damping is $c_\mathrm{S} = 0$; the torque-control loop is ideal, i.e., $G_\mathrm{t}(s) = 1$; and the speed measurement is ideal, i.e., $M(s) = 1$.

### A. Feedback Controller Design

Because the feedback controller should be able to cope with nonzero disturbance torque $T_\mathrm{L}$, the state-space model (1) is augmented with the integral state,

$$\dot{x}_\mathrm{I} = \omega_\mathrm{ref,filt} - \omega_\mathrm{M} \tag{3}$$

according to Fig. 1. When the state-feedback controller $T_\mathrm{M} = -\boldsymbol{K}\boldsymbol{x} + k_\mathrm{I}x_\mathrm{I}$ is used, the augmented closed-loop system is

$$\begin{bmatrix} \dot{\boldsymbol{x}} \\ \dot{x}_\mathrm{I} \end{bmatrix} = \underbrace{\begin{bmatrix} \boldsymbol{A} - \boldsymbol{B}_\mathrm{u}\boldsymbol{K} & \boldsymbol{B}_\mathrm{u}k_\mathrm{I} \\ -\boldsymbol{C} & 0 \end{bmatrix}}_{\boldsymbol{A}_\mathrm{cl}} \begin{bmatrix} \boldsymbol{x} \\ x_\mathrm{I} \end{bmatrix} + \begin{bmatrix} \boldsymbol{0}_{3\times 1} \\ 1 \end{bmatrix} \omega_\mathrm{ref,filt} + \begin{bmatrix} \boldsymbol{B}_\mathrm{w} \\ 0 \end{bmatrix} T_\mathrm{L} \tag{4}$$

where $\boldsymbol{C} = \begin{bmatrix}1 & 0 & 0\end{bmatrix}$ and $\boldsymbol{K} = \begin{bmatrix}k_1 & k_2 & k_3\end{bmatrix}$ is the feedback gain. Eigenvalues (poles) of the closed-loop system can be calculated from the characteristic equation $B(s) = \det(s\mathbf{I} - \boldsymbol{A}_\mathrm{cl})$. Here, the four poles of $B(s)$ are divided into two pairs of complex poles (dominant and resonant poles)

$$B(s) = \underbrace{(s^2 + 2\zeta_\mathrm{d}\omega_\mathrm{d}s + \omega_\mathrm{d}^2)}_{\text{Dominant poles}} \underbrace{(s^2 + 2\zeta_\mathrm{r}\omega_\mathrm{r}s + \omega_\mathrm{r}^2)}_{\text{Resonant poles}} \tag{5}$$

which leads to the following feedback-gain selection

$$\begin{aligned} k_\mathrm{I} &= \frac{J_\mathrm{L}J_\mathrm{M}\omega_\mathrm{d}^2\omega_\mathrm{r}^2}{K_\mathrm{S}} \\ k_1 &= 2J_\mathrm{M}(\zeta_\mathrm{d}\omega_\mathrm{d} + \zeta_\mathrm{r}\omega_\mathrm{r}) \\ k_2 &= J_\mathrm{M}(\omega_\mathrm{d}^2 + \omega_\mathrm{r}^2 + 4\zeta_\mathrm{d}\omega_\mathrm{d}\zeta_\mathrm{r}\omega_\mathrm{r}) - \frac{K_\mathrm{S}(J_\mathrm{M} + J_\mathrm{L})}{J_\mathrm{L}} - k_\mathrm{I} \\ k_3 &= \frac{2J_\mathrm{L}J_\mathrm{M}(\zeta_\mathrm{d}\omega_\mathrm{d}\omega_\mathrm{r}^2 + \zeta_\mathrm{r}\omega_\mathrm{r}\omega_\mathrm{d}^2)}{K_\mathrm{S}} - k_1 \end{aligned} \tag{6}$$

The closed-loop poles in (5) can be arbitrarily placed by deciding the undamped natural frequencies ($\omega_\mathrm{d}$ and $\omega_\mathrm{r}$) and the damping coefficients ($\zeta_\mathrm{d}$ and $\zeta_\mathrm{r}$), cf. Section III-D.

### B. State Observer Design

*1) Full-Order Observer:* The full-order state observer can be presented as

$$\dot{\hat{\boldsymbol{x}}} = \underbrace{(\boldsymbol{A} - \boldsymbol{LC})}_{\boldsymbol{A}_\mathrm{o}}\hat{\boldsymbol{x}} + \boldsymbol{B}_\mathrm{u}T_\mathrm{M,ref} + \boldsymbol{L}\omega_\mathrm{M} \tag{7}$$

where $\boldsymbol{L} = \begin{bmatrix}l_\mathrm{f1} & l_\mathrm{f2} & l_\mathrm{f3}\end{bmatrix}^\mathrm{T}$ is the observer gain. Eigenvalues of the observer can be calculated from the characteristic equation $B_\mathrm{o}(s) = \det(s\mathbf{I} - \boldsymbol{A}_\mathrm{o})$. The three poles of the observer are presented as a combination of a real pole and complex poles:

$$B_\mathrm{o}(s) = (s + \alpha_\mathrm{fo})(s^2 + 2\zeta_\mathrm{fo}\omega_\mathrm{fo}s + \omega_\mathrm{fo}^2) \tag{8}$$

This choice leads to the observer-gain selection

$$\begin{aligned} l_{\mathrm{f1}} &= \alpha_{\mathrm{fo}} + 2\zeta_{\mathrm{fo}}\omega_{\mathrm{fo}} \\ l_{\mathrm{f2}} &= 1 + \frac{J_{\mathrm{M}}}{J_{\mathrm{L}}} - \frac{J_{\mathrm{M}}(2\zeta_{\mathrm{fo}}\omega_{\mathrm{fo}}\alpha_{\mathrm{fo}} + \omega_{\mathrm{fo}}^2)}{K_{\mathrm{S}}} \\ l_{\mathrm{f3}} &= \frac{J_{\mathrm{M}}\alpha_{\mathrm{fo}}\omega_{\mathrm{fo}}^2}{K_{\mathrm{S}}} - \frac{J_{\mathrm{M}} l_{\mathrm{f1}}}{J_{\mathrm{L}}} \end{aligned} \tag{9}$$

*2) Reduced-Order Observer:* The reduced-order observer can be presented as [29]

$$\begin{aligned} \dot{\boldsymbol{x}}_{\mathrm{r}} &= \boldsymbol{A}_{\mathrm{r}}\hat{\boldsymbol{x}}_{\mathrm{ro}} + \boldsymbol{B}_{\mathrm{r}} T_{\mathrm{M,ref}} + \boldsymbol{B}_{\mathrm{y}}\omega_{\mathrm{M}} \\ \hat{\boldsymbol{x}}_{\mathrm{ro}} &= \boldsymbol{x}_{\mathrm{r}} + \boldsymbol{L}_{\mathrm{r}}\omega_{\mathrm{M}} \end{aligned} \tag{10}$$

where $\hat{\boldsymbol{x}}_{\mathrm{ro}} = \begin{bmatrix} \hat{\theta}_{\mathrm{M}} - \hat{\theta}_{\mathrm{L}} & \hat{\omega}_{\mathrm{L}} \end{bmatrix}^{\mathrm{T}}$ and

$$\begin{aligned} \boldsymbol{A}_{\mathrm{r}} &= \begin{bmatrix} \frac{l_{\mathrm{r1}} K_{\mathrm{S}}}{J_{\mathrm{M}}} & -1 \\ \frac{K_{\mathrm{S}}}{J_{\mathrm{L}}} + \frac{l_{\mathrm{r2}} K_{\mathrm{S}}}{J_{\mathrm{M}}} & 0 \end{bmatrix} \qquad \boldsymbol{B}_{\mathrm{y}} = \begin{bmatrix} 1 \\ 0 \end{bmatrix} \\ \boldsymbol{L}_{\mathrm{r}} &= \begin{bmatrix} l_{\mathrm{r1}} & l_{\mathrm{r2}} \end{bmatrix}^{\mathrm{T}} \qquad \boldsymbol{B}_{\mathrm{r}} = \boldsymbol{L}_{\mathrm{r}}/J_{\mathrm{M}} \end{aligned} \tag{11}$$

The two poles of the observer are presented as complex poles:

$$B_{\mathrm{ro}}(s) = s^2 + 2\zeta_{\mathrm{ro}}\omega_{\mathrm{ro}} s + \omega_{\mathrm{ro}}^2 \tag{12}$$

leading to the observer-gain selection

$$l_{\mathrm{r1}} = -\frac{2\zeta_{\mathrm{ro}}\omega_{\mathrm{ro}} J_{\mathrm{M}}}{K_{\mathrm{S}}} \qquad l_{\mathrm{r2}} = J_{\mathrm{M}}\left(\frac{\omega_{\mathrm{ro}}^2}{K_{\mathrm{S}}} - \frac{1}{J_{\mathrm{L}}}\right) \tag{13}$$

### *C. Prefilter Design*

The command tracking from the reference vector $\boldsymbol{r}$ to the load angular speed $\omega_{\mathrm{L}}$ is set by the prefilter,

$$\begin{aligned} \dot{\boldsymbol{x}}_{\mathrm{f}} &= \underbrace{\begin{bmatrix} -2\zeta_{\mathrm{l}}\omega_{\mathrm{l}} & -\omega_{\mathrm{l}}^2 \\ 1 & 0 \end{bmatrix}}_{\boldsymbol{A}_{\mathrm{f}}} \boldsymbol{x}_{\mathrm{f}} \\ &+ \underbrace{\begin{bmatrix} \frac{1}{\omega_{\mathrm{d}}^2} + \frac{\omega_{\mathrm{l}}^2}{\omega_{\mathrm{d}}^2\omega_{\mathrm{r}}^2} + \frac{4\zeta_{\mathrm{r}}\zeta_{\mathrm{d}}\omega_{\mathrm{l}}}{\omega_{\mathrm{d}}^2\omega_{\mathrm{r}}} & 2\left(\frac{\zeta_{\mathrm{r}}\omega_{\mathrm{l}}^2}{\omega_{\mathrm{r}}\omega_{\mathrm{d}}^2} + \frac{\zeta_{\mathrm{l}}\omega_{\mathrm{l}}}{\omega_{\mathrm{d}}^2}\right) & \frac{\omega_{\mathrm{l}}^2}{\omega_{\mathrm{d}}^2} \\ 0 & 0 & 0 \end{bmatrix}}_{\boldsymbol{B}_{\mathrm{f}}} \boldsymbol{r} \\ \omega_{\mathrm{ref,filt}} &= \underbrace{\begin{bmatrix} 2(\zeta_{\mathrm{d}}\omega_{\mathrm{d}} - \zeta_{\mathrm{l}}\omega_{\mathrm{l}}) & \omega_{\mathrm{d}}^2 - \omega_{\mathrm{l}}^2 \end{bmatrix}}_{\boldsymbol{C}_{\mathrm{f}}} \boldsymbol{x}_{\mathrm{f}} \\ &+ \underbrace{\begin{bmatrix} \frac{1}{\omega_{\mathrm{d}}^2} + \frac{\omega_{\mathrm{l}}^2}{\omega_{\mathrm{d}}^2\omega_{\mathrm{r}}^2} + \frac{4\zeta_{\mathrm{r}}\zeta_{\mathrm{d}}\omega_{\mathrm{l}}}{\omega_{\mathrm{d}}^2\omega_{\mathrm{r}}} & 2\left(\frac{\zeta_{\mathrm{r}}\omega_{\mathrm{l}}^2}{\omega_{\mathrm{r}}\omega_{\mathrm{d}}^2} + \frac{\zeta_{\mathrm{l}}\omega_{\mathrm{l}}}{\omega_{\mathrm{d}}^2}\right) & \frac{\omega_{\mathrm{l}}^2}{\omega_{\mathrm{d}}^2} \end{bmatrix}}_{\boldsymbol{D}_{\mathrm{f}}} \boldsymbol{r} \end{aligned} \tag{14}$$

where $\boldsymbol{r} = \begin{bmatrix} j_{\mathrm{ref}} & a_{\mathrm{ref}} & \omega_{\mathrm{ref}} \end{bmatrix}^{\mathrm{T}}$. The speed reference $\omega_{\mathrm{ref}}$ and its first and second time derivatives $a_{\mathrm{ref}}$ and $j_{\mathrm{ref}}$, respectively, can be generated as described, e.g., in [23], [24]. The prefilter is designed to replace the dominant dynamics ($\zeta_{\mathrm{d}}$ and $\omega_{\mathrm{d}}$) of the feedback loop with better damped and faster dynamics ($\zeta_{\mathrm{l}}$ and $\omega_{\mathrm{l}}$) and to obtain zero steady-state tracking error for step, ramp, and parabolic references [9].

### *D. Design Procedure*

The speed controller is designed through the following steps:

1) Construct the open-loop system matrices $\boldsymbol{A}$ and $\boldsymbol{B}_{\mathrm{u}}$ in (1) using the parameter estimates ($J_{\mathrm{M}}$, $J_{\mathrm{L}}$, $K_{\mathrm{S}}$). These parameter estimates can be obtained, e.g., from the manufacturers datasheet or from a parameter identification routine [28].
2) Place the dominant poles of the feedback loop, i.e., select $\omega_{\mathrm{d}}$ and $\zeta_{\mathrm{d}}$. Because the feedback loop is used only for disturbance rejection, avoid selecting too high $\omega_{\mathrm{d}}$. Select high enough damping for the dominant poles, e.g., $0.8 \leq \zeta_{\mathrm{d}} \leq 1$.
3) Place the resonant poles, i.e., select $\omega_{\mathrm{r}}$ and $\zeta_{\mathrm{r}}$. It is important to notice that if $\omega_{\mathrm{d}} > \omega_{\mathrm{ares}}$ and the feedback loop is delayed, the inertia ratio $R = J_{\mathrm{L}}/J_{\mathrm{M}}$ should be taken into account when placing the resonant poles. More information about the resonant pole selection will be provided in Section IV-D.
4) Place the observer poles by selecting the coefficients $\{\omega_{\mathrm{fo}},\ \zeta_{\mathrm{fo}},\ \alpha_{\mathrm{fo}}\}$ if the full-order observer is applied or $\{\omega_{\mathrm{ro}},\ \zeta_{\mathrm{ro}}\}$ if the reduced-order observer is applied. It is to be noted that if the observer poles are selected to be too fast, the measurement-noise amplification may become unbearable. As an example, the following selection may be applied: $\omega_{\mathrm{fo}} = \omega_{\mathrm{ro}} = \omega_{\mathrm{d}}$, $\zeta_{\mathrm{fo}} = \zeta_{\mathrm{ro}} = 1$, and $\alpha_{\mathrm{fo}} = \omega_{\mathrm{r}}$.
5) Calculate the state-feedback gains $\boldsymbol{K}$ and $k_{\mathrm{I}}$ using (6). Furthermore, calculate the full-order observer gain $\boldsymbol{L}$ using (9) or the reduced-order observer gain $\boldsymbol{L}_{\mathrm{r}}$ using (13).
6) Decide command-tracking performance by selecting $\omega_{\mathrm{l}}$ and $\zeta_{\mathrm{l}}$ and construct the prefilter matrices $\boldsymbol{A}_{\mathrm{f}}$, $\boldsymbol{B}_{\mathrm{f}}$, $\boldsymbol{C}_{\mathrm{f}}$, and $\boldsymbol{D}_{\mathrm{f}}$ using (14).
7) Discretize the continuous-time subsystems (3), (7), (10), and (14), e.g., by applying Tustin's method [30].

If there are significant time delays in the system, the stability of the closed-loop system should be checked, e.g., by applying the Nyquist diagram for the loop transfer function of the system (cf. Section IV).

## IV. DESIGN EXAMPLE

### *A. System Parameters*

System parameters, considered in the design example, are based on the experimental setup shown in Fig. 2. The setup consists of two 4-kW 2400-rpm permanent-magnet ac servo motors coupled together with a toothed belt. In order to vary the coupling stiffness, different belts can be used. An additional inertia disk can be added to the shaft of the load motor.

The torque-control loop is accomplished using field-oriented control. When the system is operating in the linear region, the closed torque-control loop can be modeled as a transfer function [31]

$$G_{\mathrm{t}}(s) = e^{-sT_{\mathrm{d}}}\frac{\alpha_{\mathrm{t}}}{s + \alpha_{\mathrm{t}}} \tag{15}$$

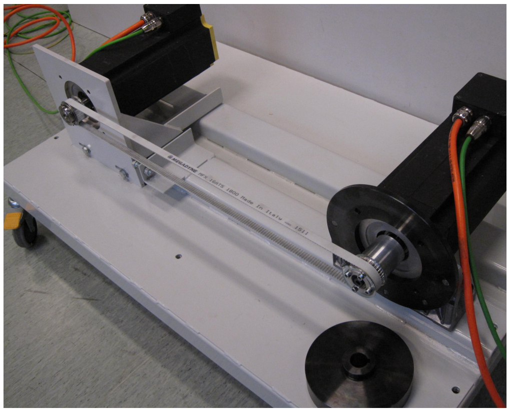

Fig. 2. Experimental setup.

TABLE I
Design Parameters and Relating Controller Gains for Different Controllers

| Design parameter | Value | Controller gain | Value |
|---|---|---|---|
| $\zeta_\mathrm{d}$ | 0.9 | $k_\mathrm{I}$(Nm/rad) | 1444 |
| $\omega_\mathrm{d}$ (rad/s) | 380 | $k_1$(Nms/rad) | 4.08 |
| $\zeta_\mathrm{r}$ | 0.1 | $k_2$(Nm/rad) | −268 |
| $\omega_\mathrm{r}$ (rad/s) | Eq. (2) | $k_3$(Nms/rad) | 3.19 |
| $\alpha_\mathrm{fo}$ (rad/s) | 663 | $k_\mathrm{p}$(Nms/rad) | 4.94 |
| $\zeta_\mathrm{fo}$ | 1 | $k_\mathrm{i}$(Nm/rad) | 832 |
| $\omega_\mathrm{fo}$ (rad/s) | 380 | $l_\mathrm{r1}$(Nm/rad) | −0.0035 |
| $\zeta_\mathrm{ro}$ | 1 | $l_\mathrm{r2}$(Nms/rad) | −0.3436 |
| $\omega_\mathrm{ro}$ (rad/s) | 380 | $l_\mathrm{f1}$(Nm/rad) | 1423 |
| $\zeta_\mathrm{l}$ | 1 | $l_\mathrm{f2}$(Nms/rad) | −0.95 |
| $\omega_\mathrm{l}$ (rad/s) | 420 | $l_\mathrm{f3}$(Nm/rad) | −988 |

where $\alpha_\mathrm{t} = 1.8$ krad/s is the bandwidth and $T_\mathrm{d} = 0.2$ ms is the time delay of the torque-control loop. The speed measurement is modelled using a time delay $M(s) = e^{-sT_\mathrm{m}}$ and noise $n$, cf. Fig. 1. The sampling period is $h = 0.5$ ms, leading to the speed-measurement delay of $T_\mathrm{m} = 0.5$ ms [10]. The variance of noise $n$ is 0.5 rad$^2$/s$^2$.[1] The feedback-loop delay is expressed as

$$G_\Delta(s) = G_\mathrm{t}(s)M(s) \tag{16}$$

Depending on the belt selection and the usage of the additional inertia disc, the mechanical-parameter values of the test system are: $J'_\mathrm{M} = 0.005$ kgm$^2$, $J'_\mathrm{L,min} = 0.005$ kgm$^2$, $J'_\mathrm{L,max} = 0.039$ kgm$^2$, $K'_\mathrm{S,max} = 1100$ Nm/rad, $K'_\mathrm{S,min} = 650$ Nm/rad, and $c'_\mathrm{S} = 0.11$ Nms/rad. Unless otherwise stated, accurate mechanical-parameter values are assumed in the following sections when designing and analyzing the controllers (i.e., $J_\mathrm{M} = J'_\mathrm{M}$, $J_\mathrm{L} = J'_\mathrm{L}$, and $K_\mathrm{S} = K'_\mathrm{S}$, which leads to $\boldsymbol{A} = \boldsymbol{A}'$ and $\boldsymbol{B}_\mathrm{u} = \boldsymbol{B}'_\mathrm{u}$). For time-domain simulations and laboratory experiments, the proposed controller was digitally implemented as described in the Appendix.

### *B. Loop Transfer Function and Measurement-Noise Amplification*

The open-loop transfer function from the torque reference $T_\mathrm{M,ref}$ to the measured motor speed $\omega_\mathrm{M}$ is

$$G(s) = \boldsymbol{C}(s\boldsymbol{I} - \boldsymbol{A}')^{-1}\boldsymbol{B}'_\mathrm{u}G_\Delta(s) \tag{17}$$

The loop transfer functions of the state-space controlled systems with a full-order observer and with a reduced-order observer are

$$\begin{aligned} H_\mathrm{fo}(s) &= \boldsymbol{K}(s\boldsymbol{I} - \boldsymbol{A} + \boldsymbol{L}\boldsymbol{C})^{-1}[\boldsymbol{L}G(s) + \boldsymbol{B}_\mathrm{u}] \\ &\quad + k_\mathrm{I}G(s)/s \qquad (18) \\ H_\mathrm{ro}(s) &= \boldsymbol{K}_\mathrm{r}(s\boldsymbol{I} - \boldsymbol{A}_\mathrm{r})^{-1}[\boldsymbol{B}_\mathrm{r} + (\boldsymbol{B}_\mathrm{y} + \boldsymbol{A}_\mathrm{r}\boldsymbol{L}_\mathrm{r})G(s)] \\ &\quad + \boldsymbol{K}_\mathrm{r}\boldsymbol{L}_\mathrm{r}G(s) + (k_\mathrm{I} + k_1)G(s)/s \qquad (19) \end{aligned}$$

respectively. The stability of the different systems will be analyzed in the following sections by means of Nyquist diagrams of these loop transfer functions. The Nyquist diagrams are depicted between the frequencies of $\omega = 0$ and $\omega = \pi/h$. The system is stable if the Nyquist diagram of the loop transfer function does not encircle the critical point (−1+j0) [29].

Moreover, the robustness of the closed speed-control loop is analyzed by applying the maximum peak criteria for the sensitivity function $S(s) = [1 + H(s)]^{-1}$, where $H(s)$ is the corresponding loop transfer function [i.e., (18) or (19)]. The maximum peak of the sensitivity function is defined as [32]

$$M_\mathrm{S} = \max_{\omega} |S(j\omega)| \tag{20}$$

Having $M_\mathrm{S} < 2$ indicates good robustness. On the other hand, if $M_\mathrm{S} > 4$, both robustness and performance are poor. It is worth noticing that, when applying the maximum peak criteria, there is no need to use the phase margin or gain margin [32]. The sensitivity function peaks are given together with the Nyquist diagrams in the following sections.

The noise amplification of the system is examined through the noise transfer function from the noise $n$ to the motor electromagnetic torque $T_\mathrm{M}$. The noise transfer functions of the state-space controlled system with a full-order observer and with a reduced-order observer are

$$\begin{aligned} N_\mathrm{fo}(s) &= -G_\mathrm{t}(s)[k_\mathrm{I}/s + \boldsymbol{K}(s\boldsymbol{I} - \boldsymbol{A})^{-1}\boldsymbol{L}] \qquad (21) \\ N_\mathrm{ro}(s) &= -G_\mathrm{t}(s)\{k_\mathrm{I}/s + k_1 \\ &\quad + \boldsymbol{K}_\mathrm{r}[(s\boldsymbol{I} - \boldsymbol{A}_\mathrm{r})^{-1}\boldsymbol{B}_\mathrm{y} + \boldsymbol{L}_\mathrm{r}]\} \qquad (22) \end{aligned}$$

respectively. The measurement-noise amplification of the different systems is compared in the following sections. Lower measurement-noise amplification indicates a better feedback-loop operation.

### *C. Observer Selection*

As mentioned before, the state feedback can be constructed applying either the full-order observer or the reduced-order observer, cf. Fig. 1. The observer type is selected based on the Nyquist diagrams of the loop transfer functions (18) and (19) and the measurement-noise amplifications (21) and (22). The feedback-loop poles are selected as shown in Table I and the estimates of the mechanical parameters, needed when calculating the controller gains, correspond to Section IV-A: $J_\mathrm{M} = J'_\mathrm{M}$, $J_\mathrm{L} = J'_\mathrm{L,min}$, and $K_\mathrm{S} = K'_\mathrm{S,max}$. Moreover, the feedback loop is delayed.

---

[1] In the experiments, $\omega_\mathrm{M}$ is measured using an incremental encoder (2500 pulses per revolution). The angular speed is calculated from the measured angular position difference within the fixed sampling period $h$. This sampling scheme leads to a significant quantization noise [10].

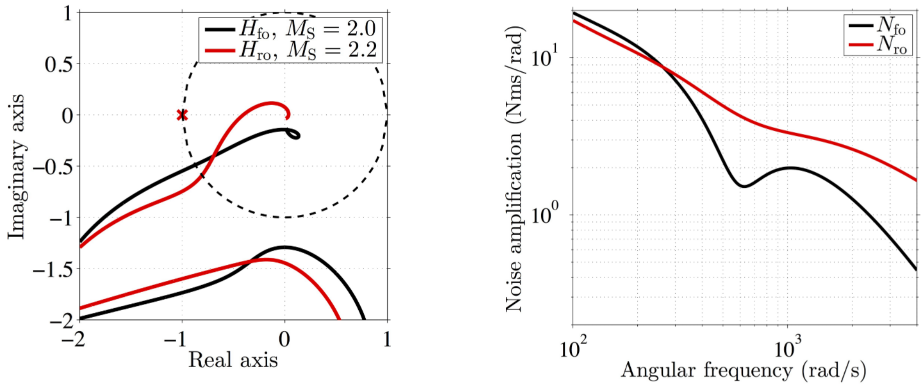

(a)

(b)

Fig. 3. (a) Nyquist diagrams of the loop transfer functions (18) and (19), and the corresponding sensitivity function peaks $M_{\mathrm{S}}$ [cf. (20)]. (b) Measurement-noise amplifications of the state-space controlled system with a full-order observer and reduced-order observer, when the feedback loop is delayed, cf. Section IV-A.

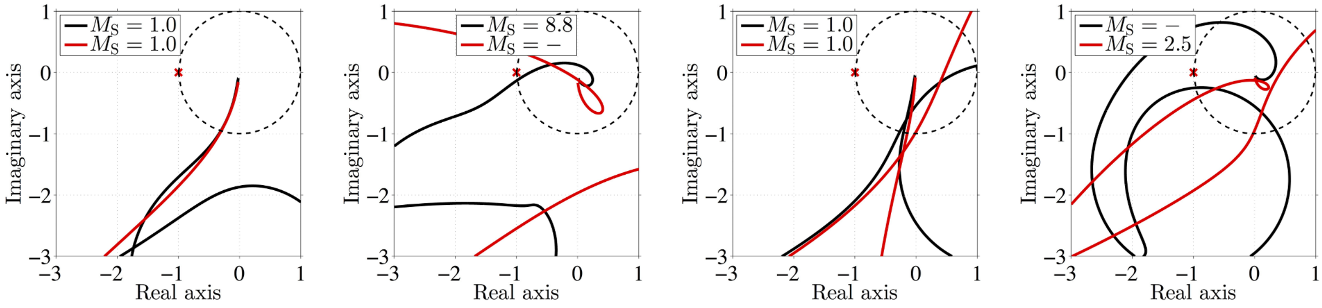

(a)

(b)

(c)

(d)

Fig. 4. Nyquist diagrams of the loop transfer function $H_{\mathrm{fo}}$ in (18) and the corresponding sensitivity function peaks $M_{\mathrm{S}}$ for different resonant-pole locations (red curve: $\omega_{\mathrm{r}} = \omega_{\mathrm{d}}$, $\zeta_{\mathrm{r}} = 0.9$; black curve: $\omega_{\mathrm{r}} = \omega_{\mathrm{res}}$, $\zeta_{\mathrm{r}} = 0.1$). (a) Inertia ratio $R = 1$ and ideal feedback loop, i.e., $G_{\Delta}(s) = 1$. (b) $R = 1$ and delayed feedback loop. (c) Inertia ratio $R = 7.8$ and ideal feedback loop. (d) $R = 7.8$ and delayed feedback loop. It it worth noticing that $\omega_{\mathrm{d}} > \omega_{\mathrm{ares}}$ is selected for both the inertia ratios.

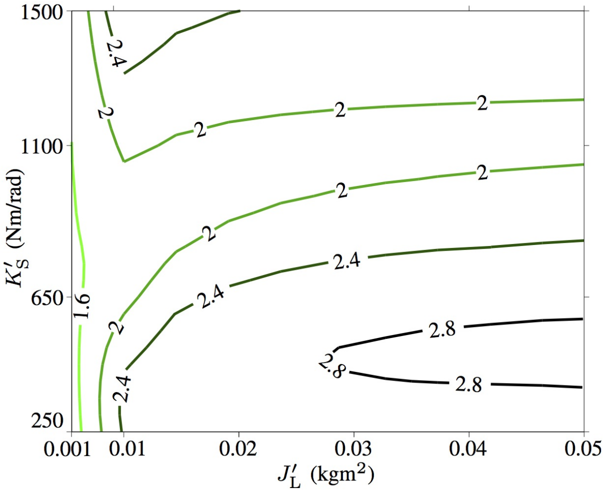

Fig. 5. Contours of the sensitivity function peaks $M_{\mathrm{S}}$, when the load inertia and coupling stiffness are varied.

Fig. 3(a) shows the Nyquist curves of the loop transfer functions. It can be seen that the minimum distance of the Nyquist curve from the critical point ($-1$+j0, marked with the red cross) is approximately the same for both the observers and the sensitivity function peaks are $M_{\mathrm{S}} \approx 2$, indicating that the both observers could be applied without difficulties. Fig. 3(b) shows the measurement-noise amplifications. It can be seen that the full-order observer suppresses the high-frequency noise much better than the reduced-order observer. Similar feedback-loop characteristics can be found with different mechanical parameters or with different state-feedback pole locations. Hence, based on these observations, the full-order observer is selected for further analysis.

### D. Selection of Resonant Poles

The selection of the resonant-pole coefficients $\omega_{\mathrm{r}}$ and $\zeta_{\mathrm{r}}$ is based on the stability analysis of the proposed state-feedback controller. The analysis is carried out for two different load-inertia values ($J_{\mathrm{L}} = 0.005$ kgm$^2$ and $J_{\mathrm{L}} = 0.039$ kgm$^2$), corresponding to the experimental setup and leading to the inertia ratios of $R = 1$ and $R = 7.8$. In order to study the effects of a fast feedback loop, the natural frequency $\omega_{\mathrm{d}}$ of the dominant feedback-loop dynamics is selected to be higher than the antiresonance frequency $\omega_{\mathrm{ares}}$. Furthermore, in order to have the same relative distance between $\omega_{\mathrm{d}}$ and $\omega_{\mathrm{ares}}$ for both the inertia ratios, $\omega_{\mathrm{d}} = 2\omega_{\mathrm{ares}}/3 + \omega_{\mathrm{res}}/3$ is chosen; the condition $\omega_{\mathrm{d}} > \omega_{\mathrm{ares}}$ is fulfilled as can be realized based on (2). The damping coefficient $\zeta_{\mathrm{d}} = 0.9$ is selected.

Fig. 4 shows the Nyquist diagrams of the loop transfer function (18) with two resonant-pole locations (red curve: $\omega_\mathrm{r} = \omega_\mathrm{d}$, $\zeta_\mathrm{r} = 0.9$; black curve: $\omega_\mathrm{r} = \omega_\mathrm{res}$, $\zeta_\mathrm{r} = 0.1$). Fig. 4(a) shows a case where the inertia ratio is $R = 1$ and the feedback loop is assumed to be ideal, i.e., $G_\Delta(s) = 1$. Fig. 4(b) shows a case where the inertia ratio is $R = 1$ and the feedback loop is delayed, cf. Section IV-A. It is worth noticing that the resonant-pole selection $\{\omega_\mathrm{r} = \omega_\mathrm{d},\ \zeta_\mathrm{r} = 0.9\}$ leads to an unstable feedback loop, whereas the selection $\{\omega_\mathrm{r} = \omega_\mathrm{res},\ \zeta_\mathrm{r} = 0.1\}$ is stable, though the peak sensitivity value $M_\mathrm{s} = 8.8$ indicates poor robustness. In practice, either the feedback-loop delay should be reduced or dynamic performance (i.e., the natural frequency $\omega_\mathrm{d}$) should be reduced in this particular case.

Fig. 4(c) shows a case where the inertia ratio is $R = 7.8$ and the feedback loop is assumed to be ideal. Fig. 4(d) shows a case where the inertia ratio is $R = 7.8$ and the feedback loop is delayed. Interestingly, in this case, the resonant-pole selection $\{\omega_\mathrm{r} = \omega_\mathrm{res},\ \zeta_\mathrm{r} = 0.1\}$ leads to an unstable feedback loop. On the other hand, the pole selection $\{\omega_\mathrm{r} = \omega_\mathrm{d},\ \zeta_\mathrm{r} = 0.9\}$ gives a stable and robust feedback-loop operation ($M_\mathrm{s} = 2.5$).

Based on Fig. 4 and on a more extensive study (where the inertia ratio was varied between $R = 0.5 \ldots 10$), it can be concluded that if the inertia ratio is small (approximately $R < 1.5$) and the feedback loop is delayed, it is beneficial to keep the closed-loop resonant poles in the vicinity of the open-loop resonant poles. On the other hand, when the inertia ratio is higher (approximately $R > 1.5$), the natural frequency $\omega_\mathrm{r}$ of the resonant poles should be lower and the damping $\zeta_\mathrm{r}$ higher. It was also found out that if the feedback loop is delayed and $\omega_\mathrm{d} < \omega_\mathrm{ares}$, it is beneficial to use $\omega_\mathrm{r} = \omega_\mathrm{res}$ and $0.05 < \zeta_\mathrm{d} < 0.1$ also with higher inertia ratios.

### *E. Feedback-Loop Robustness*

The robustness against the parameter errors is analyzed by calculating the sensitivity function peaks $M_\mathrm{S}$, when the actual load inertia $J'_\mathrm{L}$ is varied between $0.001 \ldots 0.05$ kgm$^2$ and the actual coupling stiffness $K'_\mathrm{S}$ is varied between $250 \ldots 1500$ Nm/rad. The controller gains are kept constant (Table I). Fig. 5 shows the contours of the sensitivity function peaks with the given parameter variation. The peak values $M_\mathrm{S} < 3$ indicate that the designed controller is robust against the parameter variations.

## V. BENCHMARK METHOD: PI CONTROLLER

In the following sections, the proposed state-feedback controller will be compared to the PI speed controller. The output of the PI controller is $T_\mathrm{M,ref} = C(s)(\omega_\mathrm{ref} - \omega_\mathrm{M})$, where

$$C(s) = k_\mathrm{p} + \frac{k_\mathrm{i}}{s} \tag{23}$$

and $k_\mathrm{p}$ is the proportional gain and $k_\mathrm{i}$ is the integral gain. If $\omega_\mathrm{d} < \omega_\mathrm{ares}$ is selected, the dominant poles of the PI-controlled system can be placed to equal those in (5), leading to the PI-controller gain selection [9]

$$\begin{aligned} k_\mathrm{p} &= \frac{2J_\mathrm{M}\zeta_\mathrm{d}\omega_\mathrm{d}\left[\frac{K_\mathrm{S}J}{\omega_\mathrm{d}^2 J_\mathrm{M} J_\mathrm{L}} + \frac{J_\mathrm{L}\omega_\mathrm{d}^2}{K_\mathrm{S}} + 2(2\zeta_\mathrm{d}^2 - 1)\right]}{\frac{K_\mathrm{S}}{\omega_\mathrm{d}^2 J_\mathrm{L}} + \frac{J_\mathrm{L}\omega_\mathrm{d}^2}{K_\mathrm{S}} + 2(2\zeta_\mathrm{d}^2 - 1)} \\ k_\mathrm{i} &= \frac{J_\mathrm{M}\omega_\mathrm{d}^2\left(\frac{K_\mathrm{S}J}{\omega_\mathrm{d}^2 J_\mathrm{M} J_\mathrm{L}} + \frac{J_\mathrm{L}\omega_\mathrm{d}^2}{K_\mathrm{S}} - \frac{J}{J_\mathrm{M}} + 4\zeta_\mathrm{d}^2 - 1\right)}{\frac{K_\mathrm{S}}{\omega_\mathrm{d}^2 J_\mathrm{L}} + \frac{J_\mathrm{L}\omega_\mathrm{d}^2}{K_\mathrm{S}} + 2(2\zeta_\mathrm{d}^2 - 1)} \end{aligned} \tag{24}$$

where $J = J_\mathrm{M} + J_\mathrm{L}$.

The loop transfer function of the PI-controlled system is

$$H_\mathrm{PI}(s) = C(s)G(s) \tag{25}$$

The noise transfer function is

$$N_\mathrm{PI}(s) = -G_\mathrm{t}(s)C(s) \tag{26}$$

## VI. RESULTS

### *A. Simulation Results*

The proposed state-space controller is compared to the PI controller defined in Section V by means of time-domain simulations, which are supported with the corresponding Nyquist diagrams and measurement-noise amplifications. Particularly, the load-torque rejection and sensitivities to the measurement noise, mechanical parameter errors, and torque-control loop dynamics are studied. To make a fair comparison, the coefficients ($\omega_\mathrm{d}$ and $\zeta_\mathrm{d}$) of the dominant poles are selected to be equal for both the controllers. Moreover, to be able to use the PI controller, $\omega_\mathrm{d} < \omega_\mathrm{ares}$ has to be selected. Table I shows the selected feedback-loop coefficients and the related controller gains, which are calculated using (6), (9), and (24), using the mechanical parameters $J_\mathrm{M} = J'_\mathrm{M}$, $J_\mathrm{L} = J'_\mathrm{L,min}$, and $K_\mathrm{S} = K'_\mathrm{S,max}$. Both controllers are discretized using Tustin's method.

In Fig. 6, the feedback loop is assumed to be ideal, i.e., $G_\Delta(s) = 1$. Though, the measurement noise $n$ remains. Simulation results are shown in Fig. 6(a), where the speed reference is zero and a 10-Nm stepwise loading torque is applied at $t = 0.02$ s. According to the Nyquist diagrams and the sensitivity function peaks, shown in Fig. 6(b), both the proposed controller and PI controller could be applied without difficulties. However, the measurement-noise amplification, shown in Fig. 6(c), favours the selection of the proposed state-space controller. It can be seen that the time-domain simulation results in Fig. 6(a) agree well with the frequency-domain analysis.

In Fig. 7, the feedback loop is delayed, cf. Section IV-A. It can be seen in Fig. 7(b) that the PI-controlled system is close to be unstable, because the loop transfer function curve almost encircles the critical point. This is also indicated with the high value $M_\mathrm{S} = 7.9$ of the sensitivity function peak. However, the proposed state-space controller remains stable and the sensitivity function peak $M_\mathrm{S} = 2.0$ indicates good robustness. Moreover, the measurement-noise amplification of the state-space controller is lower.

In Fig. 8, the effect of the mechanical parameter errors on the stability of the system is examined by increasing the load

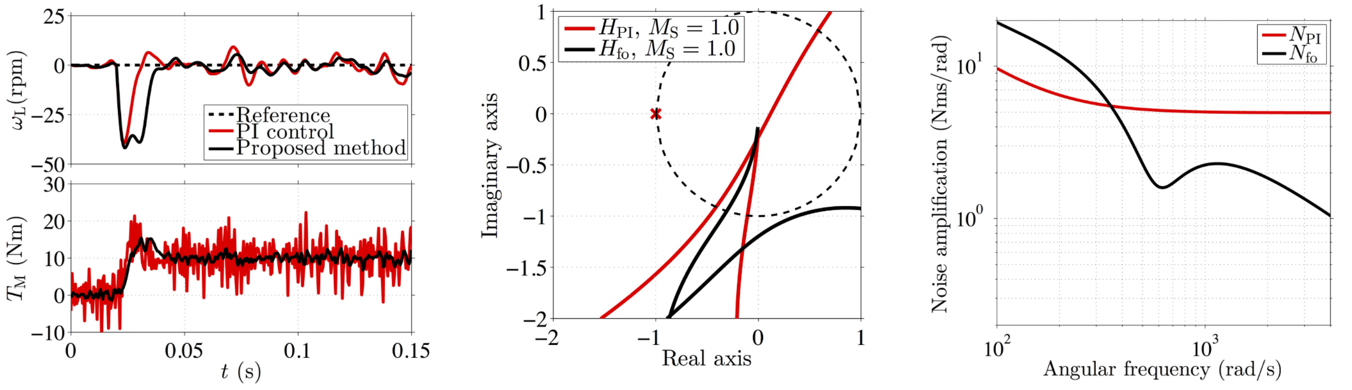

(a) (b) (c)

Fig. 6. Ideal feedback loop, i.e., $G_{\Delta}(s) = 1$: (a) simulated load-torque rejection; (b) Nyquist curve and the sensitivity function peak $M_{\mathrm{S}}$; (c) noise amplification of the control system.

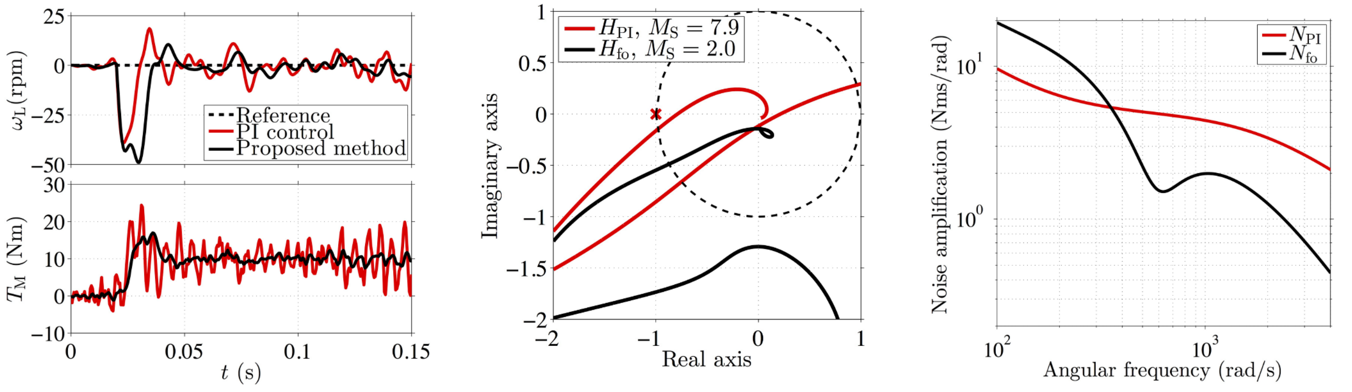

(a) (b) (c)

Fig. 7. Effect of the current-control loop and speed measurement dynamics: (a) simulated load-torque rejection; (b) Nyquist curve and the sensitivity function peak $M_{\mathrm{S}}$; (c) noise amplification of the control system.

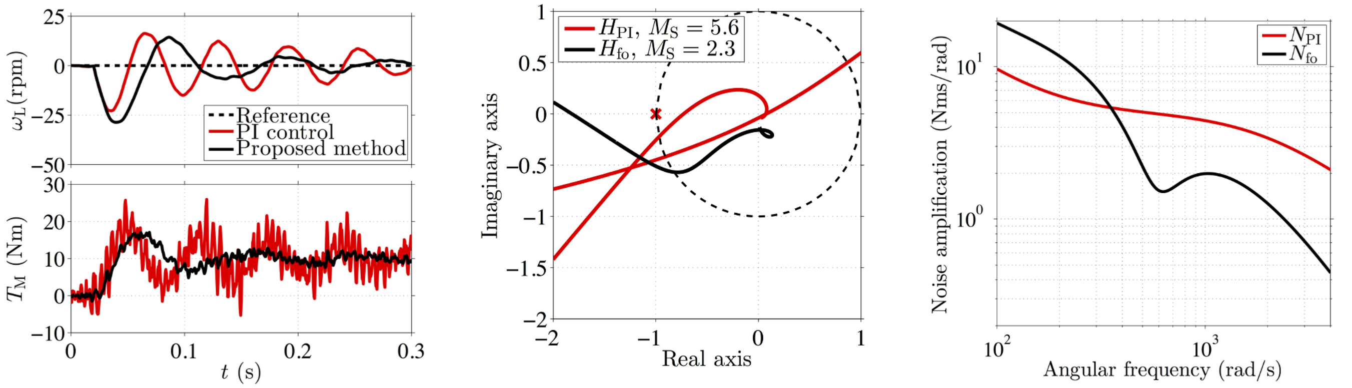

(a) (b) (c)

Fig. 8. Effect of the mechanical parameter errors: (a) simulated load-torque rejection; (b) Nyquist curve and the sensitivity function peak $M_{\mathrm{S}}$; (c) noise amplification of the control system.

inertia to $J'_{\mathrm{L,max}}$ and reducing the coupling stiffness to $K'_{\mathrm{S,min}}$. It is worth noticing that the estimated values of $J_{\mathrm{L}}$ and $K_{\mathrm{S}}$, which are used for the controller tuning, are kept unchanged. Other parameters are kept in their nominal values. It can be seen in Fig. 8(b) that both the systems remain stable but the state-space controller is a more robust option according to the lower sensitivity function peak $M_{\mathrm{S}} = 2.3$. Again, the noise amplification of the state-space controlled system is clearly lower.

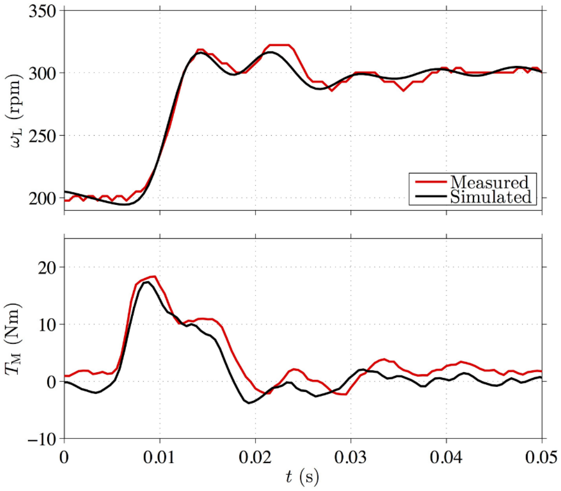

Fig. 9. Experimental and simulated step responses of the proposed 2DOF controller.

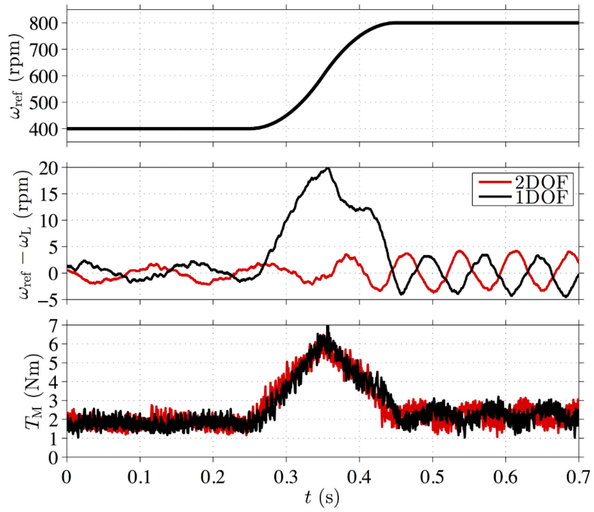

Fig. 10. Experimental parabolic-command tracking of the proposed controller.

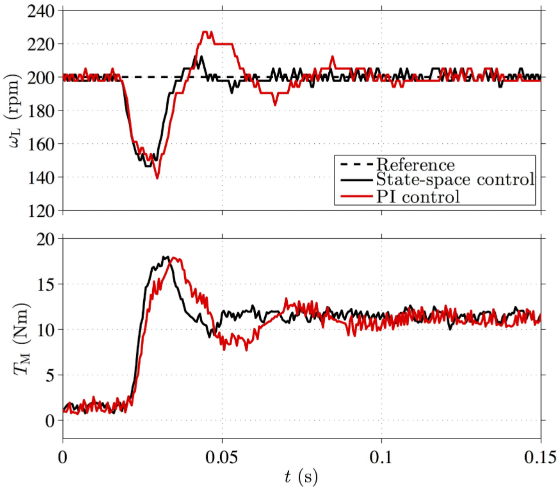

Fig. 11. Experimental load-torque rejection.

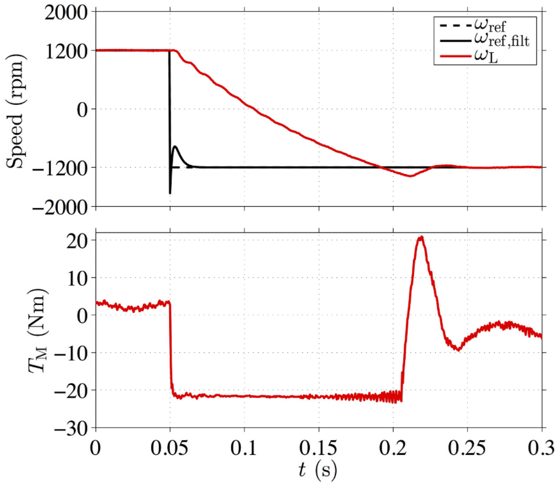

Fig. 12. Experimental step response of the proposed 2DOF controller, when a rated-speed step is applied.

## B. *Experimental Results*

Experiments were carried out using the setup described in Section IV-A. The step-command tracking of the proposed controller is evaluated both experimentally and by means of simulations (using the same model as in Section VI-A). The results are shown in Fig. 9. It can be seen that the proposed 2DOF state-space controller gives a fast response. Furthermore, the simulation results agree well with the experimental results.

Experimental results of the parabolic-command tracking test are shown in Fig. 10. In order to illustrate the effect of the 2DOF controller structure in command tracking, the test was carried out without the prefilter (1DOF structure) and with the prefilter (2DOF strucure). It can be seen that the command-tracking error can be almost completely removed, when using the 2DOF structure (i.e., when the prefilter is applied). Similar command-tracking performance could be achieved by applying the PI-type feedback controller together with the prefilter, according to [9]. It is worth noticing that the sine signal, appearing in the speed error and in the torque in Fig. 10, is not caused by the speed controller. Instead, an eccentric assembly of the speed encoder causes the problem. The amplitude and the frequency of this sine depend on the rotational speed.

However, as discussed in Section VI-A, when applying the PI controller, the feedback loop is more sensitive to the time delay and to the measurement noise. Fig. 11 shows the comparison of the measured load-torque rejection for the PI controller and the proposed state-space controller. The test was completed at the speed of 200 rpm. It is to be noted that, in order to obtain similar measurement-noise amplification and similar sensitivity function peak value for both the controllers, the PI controller gains are recalculated using $\omega_d = 150$ rad/s and $\zeta_d = 0.4$. Fig. 11 shows that the proposed state-space controller outperforms the PI controller in the load-torque rejection. It is worth noticing that the corresponding simulation results can be found in Fig. 7(a) for the state-space controller.

The aforementioned experimental results are obtained, when the controller is operating in the linear region. Nonetheless, the discrete-time implementation, given in the Appendix, includes also the anti-windup. Fig. 12 shows the speed reference $\omega_{\mathrm{ref,filt}}$, obtained from (14), and the load-speed response from a test, where the speed reference is stepped from 1200 rpm (half rated) to $-1200$ rpm (half rated) at $t = 0.05$ s and the maximum torque $T_{\mathrm{c,max}} = 22$ Nm in (28). It can be seen that the anti-windup is operating well. The undershoot in the speed at around $t = 0.21$ s could be reduced, by modifying the damping $\zeta_{\mathrm{d}}$ of the dominant feedback-loop poles or by modifying the anti-windup gain $1/k_1$, cf. the Appendix. Moreover, it can be seen that the speed reference $\omega_{\mathrm{ref,filt}}$ remains in reasonable limits even though a rated speed-step is requested.

## VII. CONCLUSIONS

A systematic design method for 2DOF state-space speed control of two-mass mechanical systems is presented. The design rules for the state-space controller (including the feedback gain, the full-order observer, the reduced-order observer, and the prefilter) are derived using model-based pole-placement methods. Sensitivity to the measurement noise and feedback-loop time delay were analyzed by means of Nyquist diagrams, noise transfer functions, and time-domain simulations. It was found out that the full-order observer based state-feedback controller is a preferable option. Simulations and experiments showed that the designed controller gives good reference tracking for step and dynamic commands as well as robust and fast load-torque rejection. Furthermore, it was shown that the measurement-noise rejection capability of the proposed state-space controller is superior to that of the PI controller (for given dynamic performance).

## APPENDIX
## DIGITAL IMPLEMENTATION

When the state feedback is constructed from the estimated states and the integral state is augmented with anti-windup, i.e., $T_{\mathrm{M}} = -\boldsymbol{K}\hat{\boldsymbol{x}} + k_{\mathrm{I}} x_{\mathrm{I}}$ and $\dot{x}_{\mathrm{I}} = \omega_{\mathrm{ref,filt}} - \omega_{\mathrm{M}} + (T_{\mathrm{M,ref}} - T_{\mathrm{M}})/k_1$, the controller subsystems (3), (7), and (14) can be presented as

$$\begin{aligned} \dot{\boldsymbol{x}}_{\mathrm{c}} &= \boldsymbol{A}_{\mathrm{c}} \boldsymbol{x}_{\mathrm{c}} + \boldsymbol{B}_{\mathrm{c}} \boldsymbol{u}_{\mathrm{c}} \\ T_{\mathrm{c}} &= \boldsymbol{C}_{\mathrm{c}} \boldsymbol{x}_{\mathrm{c}} \end{aligned} \tag{27}$$

where $\boldsymbol{u}_{\mathrm{c}} = \begin{bmatrix} \boldsymbol{r}^{\mathrm{T}} & \omega_{\mathrm{M}} & T_{\mathrm{M,ref}} \end{bmatrix}^{\mathrm{T}}$ is the controller input vector and $T_{\mathrm{c}}$ is the controller output. The anti-windup gain is selected as $1/k_1$ (comparable to $1/k_{\mathrm{p}}$ for a traditional PI controller). The saturated controller output $T_{\mathrm{M,ref}}$ is

$$T_{\mathrm{M,ref}} = \begin{cases} T_{\mathrm{c}}, & \text{if } |T_{\mathrm{c}}| \le T_{\mathrm{c,max}} \\ T_{\mathrm{c,max}} \operatorname{sgn}(T_{\mathrm{c}}), & \text{if } |T_{\mathrm{c}}| > T_{\mathrm{c,max}} \end{cases} \tag{28}$$

where $T_{\mathrm{c,max}}$ is the maximum torque and $\operatorname{sgn}(\cdot)$ the signum function. According to (3), (7), and (14), the controller states are selected as $\boldsymbol{x}_{\mathrm{c}} = \begin{bmatrix} \hat{\boldsymbol{x}}^{\mathrm{T}} & x_{\mathrm{I}} & \boldsymbol{x}_{\mathrm{f}}^{\mathrm{T}} \end{bmatrix}^{\mathrm{T}}$, leading to

$$\begin{aligned} \boldsymbol{A}_{\mathrm{c}} &= \begin{bmatrix} \boldsymbol{A} - \boldsymbol{L}\boldsymbol{C} & \boldsymbol{0}_{3\times 1} & \boldsymbol{0}_{3\times 2} \\ \boldsymbol{K}/k_1 & k_{\mathrm{I}}/k_1 & \boldsymbol{C}_{\mathrm{f}} \\ \boldsymbol{0}_{2\times 3} & \boldsymbol{0}_{2\times 1} & \boldsymbol{A}_{\mathrm{f}} \end{bmatrix} \\ \boldsymbol{B}_{\mathrm{c}} &= \begin{bmatrix} \boldsymbol{0}_{3\times 3} & \boldsymbol{L} & \boldsymbol{B}_{\mathrm{u}} \\ \boldsymbol{D}_{\mathrm{f}} & -1 & 1/k_1 \\ \boldsymbol{B}_{\mathrm{f}} & \boldsymbol{0}_{2\times 1} & \boldsymbol{0}_{2\times 1} \end{bmatrix} \\ \boldsymbol{C}_{\mathrm{c}} &= \begin{bmatrix} -\boldsymbol{K} & k_{\mathrm{I}} & \boldsymbol{0}_{1\times 2} \end{bmatrix} \end{aligned} \tag{29}$$

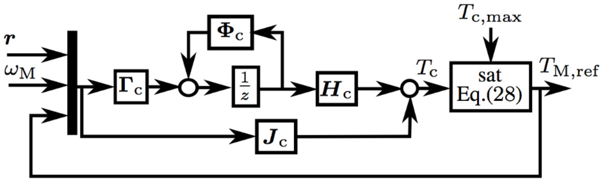

Fig. 13. Digital implementation of the proposed controller.

The discrete-time implementation of the proposed controller is shown in Fig. 13. The discrete-time matrices $\boldsymbol{\Phi}_{\mathrm{c}}$, $\boldsymbol{\Gamma}_{\mathrm{c}}$, $\boldsymbol{H}_{\mathrm{c}}$, and $\boldsymbol{J}_{\mathrm{c}}$ are obtained using Tustin's method [30].

## ACKNOWLEDGMENT

This work was supported by ABB Oy Drives. The authors are grateful to Dr. Markku Jokinen and Mr. Matti Mustonen for their insightful comments.

## REFERENCES

[1] K. Ohishi and R. Furusawa, "Actuators for motion control: Fine actuator force control for electric injection molding machines," *IEEE Ind. Electron. Mag.*, vol. 6, no. 1, pp. 4–13, Mar. 2012.

[2] M. Iwasaki, K. Seki, and Y. Maeda, "High-precision motion control techniques: A promising approach to improving motion performance," *IEEE Ind. Electron. Mag.*, vol. 6, no. 1, pp. 32–40, Mar. 2012.

[3] M. Östring, S. Gunnarsson, and M. Norrlöf, "Closed-loop identification of an industrial robot containing flexibilities," *Control Engineering Practice*, vol. 11, no. 3, pp. 291–300, 2003.

[4] R. Dhaouadi, K. Kubo, and M. Tobise, "Two-degree-of-freedom robust speed controller for high-performance rolling mill drives," *IEEE Trans. Ind. Appl.*, vol. 29, no. 5, pp. 919–926, Sep./Oct. 1993.

[5] G. Ellis and R. Lorenz, "Resonant load control methods for industrial servo drives," in *Conf. Rec. IEEE-IAS Annu. Meeting*, vol. 3, Rome, Italy, Oct. 2000, pp. 1438–1445.

[6] S. Thomsen, N. Hoffmann, and F. W. Fuchs, "PI control, PI-based state space control, and model-based predictive control for drive systems with elastically coupled loads — a comparative study," *IEEE Trans. Ind. Electron.*, vol. 58, no. 8, pp. 3647–3657, Aug. 2011.

[7] G. Zhang and J. Furusho, "Speed control of two-inertia system by PI/PID control," *IEEE Trans. Ind. Electron.*, vol. 47, no. 3, pp. 603–609, Jun. 2000.

[8] K. Szabat and T. Orlowska-Kowalska, "Vibration suppression in a two-mass drive system using PI speed controller and additional feedbacks — comparative study," *IEEE Trans. Ind. Electron.*, vol. 54, no. 2, pp. 1193–1206, Apr. 2007.

[9] S. E. Saarakkala, M. Hinkkanen, and K. Zenger, "Speed control of two-mass mechanical loads in electric drives," in *Proc. IEEE ECCE'12*, vol. 1, Raleigh, NC, Sept. 2012, pp. 1246–1253.

[10] R. Muszynski and J. Deskur, "Damping of torsional vibrations in high-dynamic industrial drives," *IEEE Trans. Ind. Electron.*, vol. 57, no. 2, pp. 544–552, Feb. 2010.

[11] W. Li and Y. Hori, "Vibration suppression using single neuron-based PI fuzzy controller and fractional-order disturbance observer," *IEEE Trans. Ind. Electron.*, vol. 54, no. 1, pp. 117–126, Feb. 2007.

[12] T. Ohmae, T. Matsuda, M. Kanno, K. Saito, and T. Sukegawa, "A microprocessor-based motor speed regulator using fast-response state observer for reduction of torsional vibration," *IEEE Trans. Ind. Appl.*, vol. IA-23, no. 5, pp. 863–871, Sept. 1987.

[13] T. Atsumi, A. Okuyama, and M. Kobayashi, “Track-following control using resonant filter in hard disk drives,” *IEEE/ASME Trans. Mechatronics*, vol. 12, no. 4, pp. 472–479, Aug. 2007.

[14] S. N. Vukosavic and M. R. Stojic, “Suppression of torsional oscillations in a high-performance speed servo drive,” *IEEE Trans. Ind. Electron.*, vol. 45, no. 1, pp. 108–117, Feb. 1998.

[15] W. C. Messner, “Classical control revisited: Variations on a theme,” in *Proc. IEEE AMC’08*, vol. 1, Trento, Italy, Mar. 2008, pp. 15–20.

[16] Y. Hori, H. Iseki, and K. Sugiura, “Basic consideration of vibration suppression and disturbance rejection control of multi-inertia system using SFLAC (state feedback and load acceleration control),” *IEEE Trans. Ind. Appl.*, vol. 30, no. 4, pp. 889–896, Jul./Aug. 1994.

[17] J.-K. Ji and S.-K. Sul, “Kalman filter and LQ based speed controller for torsional vibration suppression in a 2-mass motor drive system,” *IEEE Trans. Ind. Electron.*, vol. 42, no. 6, pp. 564–571, Dec. 1995.

[18] A. Hace, K. Jezernik, and A. Sabanovic, “SMC with disturbance observer for a linear belt drive,” *IEEE Trans. Ind. Electron.*, vol. 54, no. 6, pp. 3402–3412, Dec. 2007.

[19] D. A. Bristow, M. Tharayil, and A. G. Alleyne, “A survey of iterative learning control,” *IEEE Cont. Sys. Mag.*, vol. 26, no. 3, pp. 96–114, June 2006.

[20] G. Ellis, *Control System Design Guide: A Practical Guide*. San Diego, CA: Elsevier, 2004.

[21] K. Saiki, A. Hara, K. Sakata, and H. Fujimoto, “A study on high-speed and high-precision tracking control of large-scale stage using perfect tracking control method based on multirate feedforward control,” *IEEE Trans. Ind. Electron.*, vol. 57, no. 4, pp. 1393–1400, Apr. 2010.

[22] T. Atsumi, “Feedforward control using sampled-data polynomial for track seeking in hard disk drives,” *IEEE Trans. Ind. Electron.*, vol. 56, no. 5, pp. 1338–1346, May 2009.

[23] S. Macfarlane and E. A. Croft, “Jerk-bounded manipulator trajectory planning: design for real-time applications,” *IEEE Trans. Robot. Autom.*, vol. 19, no. 1, pp. 42–52, Feb. 2003.

[24] H. Li, M. D. Le, Z. M. Gong, and W. Lin, “Motion profile design to reduce residual vibration of high-speed positioning stages,” *IEEE/ASME Trans. Mechatronics*, vol. 14, no. 2, pp. 264–269, Apr. 2009.

[25] B.-H. Chang and Y. Hori, “Trajectory design considering derivative of jerk for head-positioning of disk drive system with mechanical vibration,” *IEEE/ASME Trans. Mechatronics*, vol. 11, no. 3, pp. 273–279, June 2006.

[26] M. Hirata, T. Hasegawa, and K. Nonami, “Seek control of hard disk drives based on final-state control taking account of the frequency components and the magnitude of control input,” in *Proc. IEEE AMC’02*, vol. 1, Maribor, Slovenia, Mar. 2002, pp. 40–45.

[27] S. Thomsen and F. W. Fuchs, “Design and analysis of a flatness-based control approach for speed control of drive systems with elastic couplings and uncertain loads,” in *Proc. EPE’11*, Birmingham, UK, Aug. 2011.

[28] S. E. Saarakkala, T. Leppinen, M. Hinkkanen, and J. Luomi, “Parameter estimation of two-mass mechanical loads in electric drives,” in *Proc. IEEE AMC’12*, Sarajevo, Bosnia and Hertsegovina, Mar. 2012.

[29] G. F. Franklin, J. D. Powell, and A. Emami-Naeini, *Feedback Control of Dynamic Systems*, 4th ed. Upper Saddle River, NJ: Prentice-Hall, 2002.

[30] G. F. Franklin, J. D. Powell, and M. L. Workman, *Digital Control of Dynamic Systems*, 3rd ed. Menlo Park, CA: Addison-Wesley, 1997.

[31] L. Harnefors and H.-P. Nee, “Model-based current control of ac machines using the internal model control method,” *IEEE Trans. Ind. Appl.*, vol. 34, no. 1, pp. 133–141, 1998.

[32] S. Skogestad and I. Postlethwaite, *Multivariable Feedback Control: Analysis and Design*. Chichester, U.K.: John Wiley & Sons, 1996.

**Seppo E. Saarakkala** received the M.Sc.(Eng.) degree from the Lappeenranta University of Technology, Lappeenranta, Finland, in 2008.

Since 2010, he has been with the Aalto University School of Electrical Engineering. He is currently a Research Scientist in the Aalto University School of Electrical Engineering, Espoo, Finland. His main research interest is the motion control of electric drives.

**Marko Hinkkanen** (M’06–SM’13) received the M.Sc.(Eng.) and D.Sc.(Tech.) degrees from the Helsinki University of Technology, Espoo, Finland, in 2000 and 2004, respectively.

Since 2000, he has been with the Helsinki University of Technology (part of Aalto University, Espoo, since 2010). He is currently an Assistant Professor with the Aalto University School of Electrical Engineering. His research interests include power-electronic converters, electric machines, and electric drives.